JPhys Energy

PURPOSE-LED PUBLISHING™

PAPER • OPEN ACCESS

Electron localization and mobility in layered $Cs_3Bi_2Br_9$ perovskite: consequences on photocatalytic processes

To cite this article: Michele Loriso *et al* 2026 *J. Phys. Energy* **8** 015009

Journal of Physics: Energy

PAPER

Electron localization and mobility in layered $Cs_3Bi_2Br_9$ perovskite: consequences on photocatalytic processes

Michele Loriso[1], Sohail Azmat[2], Andrea Listorti[2], Alessandro Landi[3], Julia Wiktor[4], Filippo De Angelis[5,6,7], Andrea Peluso[3], Silvia Colella[8] and Francesco Ambrosio[1,3,*]

[1] Dipartimento di Scienze di Base e Applicate (DISBA), Università degli Studi della Basilicata, Viale dell'Ateneo Lucano, 10 - 85100 Potenza, Italy
[2] Dipartimento di Chimica, Università degli Studi di Bari 'Aldo Moro', 70126 Bari, Italy
[3] Dipartimento di Chimica e Biologia Adolfo Zambelli, Università di Salerno, Via Giovanni Paolo II, I-84084 Fisciano (SA), Italy
[4] Department of Physics, Chalmers University of Technology, SE-412 96 Gothenburg, Sweden
[5] Department of Chemistry, Biology and Biotechnology, University of Perugia, Via Elce di Sotto 8, 06123 Perugia, Italy
[6] Computational Laboratory for Hybrid/Organic Photovoltaics (CLHYO), Istituto CNR di Scienze e Tecnologie Chimiche 'Giulio Natta' (CNR-SCITEC), Via Elce di Sotto 8, 06123 Perugia, Italy
[7] SKKU Institute of Energy Science and Technology (SIEST), Sungkyunkwan University, Suwon 440-746, Republic of Korea
[8] CNR NANOTEC—Istituto di Nanotecnologia—c/o Dipartimento di Chimica, Università degli Studi di Bari 'Aldo Moro', 70126 Bari, Italy
* Author to whom any correspondence should be addressed.

E-mail: francesco.ambrosio@unibas.it

Keywords: electronic-structure calculations, electron mobility, molecular dynamics simulations, layered perovskites for photocatalysis, small polarons

Supplementary material for this article is available online

OPEN ACCESS

RECEIVED
30 September 2025

REVISED
7 November 2025

ACCEPTED FOR PUBLICATION
19 November 2025

PUBLISHED
4 December 2025

Abstract

We study the electronic properties of lead-free layered $Cs_3Bi_2Br_9$ (CBB) perovskite, which has recently emerged as a promising material for photocatalysis. Our investigation, prompted by optical measurements suggesting self-trapping of excess charges and corroborated by *ab initio* electronic-structure calculations and molecular dynamics simulations, reveals that photogenerated electrons are assimilated in the material as small polarons, a consequence of sizable structural reorganization of both the inorganic sublattice and of A-site cations. The electron polaron exhibits an energy level at 0.6 eV below the conduction band edge, which is consistent with the physical picture ensuing from spectroscopy, and is suitably aligned with respect to redox potentials associated with common photoreduction processes. Estimation of the electron mobility, in the framework of polaron hopping, indicates a remarkable anisotropy, with interlayer movement of electron polarons being at least two orders of magnitude slower than intralayer diffusion. This suggests that heterojunctions, separating holes and electrons, are the most viable architecture to exploit CBB for photocatalysis, and that morphology as well as loading and size of CBB nanostructures are key in determining whether photogenerated electrons might reach the relevant interface or be lost due to recombination.

1. Introduction

The global pursuit of climate neutrality, coupled with the increasing demand for energy, is driving the development of novel materials for the sustainable production of green fuels—such as hydrogen (H_2) via water splitting—to reduce the dependence on fossil fuels [1, 2]. Among the wide range of green methods that have been proposed to produce high value-added chemicals, one of the most ambitious is surely heterogeneous photocatalysis [3–6]. Its working principle relies on the use of solar energy captured by a semiconducting material, the photocatalyst, to induce chemical reactions at its interface with the reactants, typically immersed in an aqueous environment [6]. Reaching an efficiency sufficient to allow for large-scale applications depends upon the fulfillment of a wide set of requirements. If we only focus on the semiconductor to be employed as a photocatalyst, these include but are not limited to:

(i) long lifetimes and high mobility of charge carriers [7–9], (ii) alignment of the semiconductor band edges with the electrochemical potentials associated with redox reactions to be catalyzed—e.g. reduction (H_2O/H_2) and oxidation (O_2/H_2O) reactions for water splitting [10–14]—and (iii) semiconductor stability in aqueous environment [12, 13, 15, 16]. Therefore, notwithstanding the rich diversity in candidate semiconductors, which sees an incessant expansion also thanks to recent advances in machine-assisted material discovery [17–19], an optimal solution has not been found yet.

In this context, metal halide perovskites (MHPs), which have emerged in the last 20 years as a valid alternative to silicon for photovoltaics [20–23], have started to show their potential also in photocatalysis. Indeed, archetypal tin and lead-based perovskites were found to suffer from issues, such as moisture sensitivity, facile oxidation, and metal leakages in the environment (particularly noxious in the case of lead), which prevented from their use in heterogeneous photocatalysis [24–26]. Alternatives, such as double perovskites, although displaying improved stability, typically feature an indirect band gap, low absorption coefficients and require careful tailoring of defects to achieve desirable properties [27]. However, the recent synthesis of lead-free *and* water-stable MHPs has sparkled a novel interest towards photocatalytic applications of this class of materials, in virtue of their outstanding and highly tunable electronic properties coupled with inexpensive manufacturing costs [28, 29]. While pioneering work on the subject achieved long-term stability only when using highly concentrated halogen acid solution [30, 31] (to avoid halogen loss) and/or overlayers/encapsulation [32, 33] (to avoid material's degradation), recently synthesized perovskites not only overcome such limitations but also show promising photocatalytic activity for a plethora of redox reactions [34–40]. These results, in some cases, have been rationalized in terms of unconventional reaction mechanisms involving polaron formation at the heterogeneous interface [41, 42], in a fashion similar to what has been recently observed also for transition metal oxides [43]. In this framework, vacancy-ordered layered perovskites are considered to be among the most promising MHPs for photocatalysis [44–46]. These materials feature trivalent metal ions, typically Bi^{3+} or Sb^{3+}, instead of the commonly used divalent Pb^{2+} and Sn^{2+}. For this reason, they do not crystallize within the usual tridimensional structure, typical of ABX_3 perovskites [47], where B is a divalent metal, X is a halide and A is the so-called A-site cation, either inorganic (e.g. Cs^+) or organic (e.g. methylammonium). Instead, they form quasi two-dimensional layers with the $A_3B_2X_9$ stoichiometry, while the bulk material is indicated as $A_3B_2[]X_9$ where [] signals the presence of ordered, interlayer B vacancies, preserving the charge neutrality. One important example is $Cs_3Bi_2[]Br_9$ (CBB in the following), which is one of the most studied compound in this class of materials [44–46, 48]. CBB features a layered structure composed of corner-sharing $BiBr_6^{3+}$ octahedra, with Cs cations occupying the resulting cuboidal cages (figure 1(a)).

When used in heterojunctions with other semiconductors (e.g. g-C_3N_4 [35]), CBB has proved to boost the efficiency of several photocatalytic processes, including water splitting [35, 49], CO_2 reduction [49–51], and degradation of organic molecules [52–54]. Furthermore, halogen substitution, metal alloying with Sb, and doping have been deployed to improve the performance of CBB and extend its application also to light-emitting devices [55–60]. Nevertheless, some aspects of the experimental findings have not been properly understood, in particular the puzzling trend observed for the efficiency versus CBB perovskite loading in the heterojunction: this features a maximum, usually at low loadings and then a steep decrease at higher perovskite concentrations [35, 49]. It has been suggested that polaronic localization in CBB may play a role in this phenomenon [35] but an in-depth characterization of the polaron energy levels at room temperature, which is necessary considering the soft nature of the lattice in this material, has not been achieved yet. Furthermore, the origin of the anisotropy in transport properties, which has been suggested by experiments and calculations in affine materials [61, 62], has not been elucidated. Nevertheless, such a knowledge is necessary to understand measurements and assist the design of more efficient photocatalysts and heterojunctions.

We here investigate the electronic properties of layered CBB with a focus on the formation and transport of electron polarons. Building on spectroscopic observations of self-trapping of charge carriers upon photoexcitation, we employ electronic-structure calculations and molecular dynamics simulations based on hybrid density functional theory (DFT) to demonstrate that photogenerated electrons localize as small polarons, stabilized by structural rearrangements involving both the inorganic sublattice and A-site cations. We further characterize the energetics of the polaronic state, which is found at 0.6 eV below the conduction band of CBB, and it is suitably aligned with redox potentials relevant to photocatalytic reduction processes. To address transport, we combine polaron hopping theory with kinetic Monte Carlo simulations, revealing a pronounced anisotropy in electron mobility: interlayer diffusion is found to be significantly slower than the intralayer process. Given the sluggish intralayer mobility, excessive thickness along the stacking direction should be avoided, as electrons generated deep within the bulk of the material may recombine before reaching the reactive interfaces and are unlikely to contribute effectively

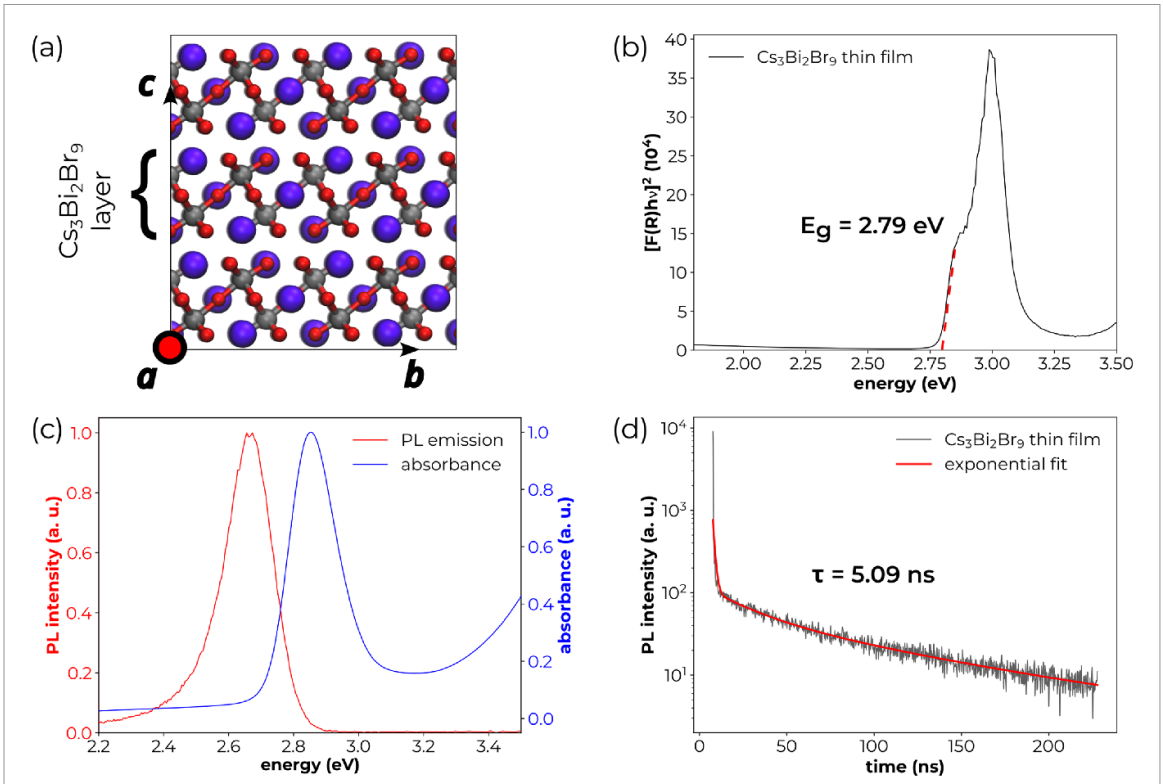

Figure 1. (a) Stick and ball representation of the tetragonal supercell employed to model $Cs_3Bi_2[\ ]Br_9$ (CBB). Bismuth in grey, bromine in red and cesium in violet. (b) Tauc plot for direct band gap evaluation, calculated using the Kubelka–Munk function from diffuse reflectance data (see main text). (c) Normalized photoluminescence and absorbance spectra of CBB thin film. (d) Photoluminescence emission decay and exponential fit for as prepared CBB thin film.

to photocatalysis. We also examine the role of intercalating defects, showing that Bi interstitials can even worsen transport as they form deep traps in the gap. Taken together, our results establish a microscopic picture of charge localization and transport in CBB and highlight the growth, structural, and morphological factors that must be considered to optimize its photocatalytic performance.

The article is organized as follows: in section 2 we discuss the spectroscopic characterization of CBB thin film; in section 3, we demonstrate, via *ab initio* simulations, the occurrence of small electron polarons in CBB and discuss the related energy levels; transport properties of the electron polarons are analyzed in section 4. Finally, the conclusions are drawn in section 5.

2. Spectroscopic characterization of CBB

We first briefly discuss the optical properties of a 150 ± 5 nm CBB thin film, which has been synthetized under stoichiometric conditions (see section S1 of the supplementary information (SI) for details of the synthesis). We here employ diffuse reflectance spectroscopy (DRS), as well as steady-state and time-resolved photoluminescence (PL) spectroscopy (see section S1 of SI). DRS is employed to record the percentage reflectance ($\%R$) of the CBB thin film, as shown in figure S1. The reflectance, R, is measured and converted into the Kubelka–Munk function (KM) using the following formula:

$$KM = \frac{(1-R)^2}{2R} \tag{1}$$

The KM function is proportional to the absorption coefficient and is used to evaluate the optical band gap of the CBB thin film. A Tauc plot is constructed by assuming a direct allowed transition, as shown in figure 1(b). The plot reveals an optical band gap of approximately 2.79 eV, indicating that the CBB thin film exhibits strong absorption and efficient electron excitation in the visible region [60, 63]. The optical gap is excitonic in nature as CBB is known to display an exciton binding energy of ≈ 0.3 eV [64]. In a previous report, some of us found that the optical band gap of CBB powders synthesized by chemical and mechanical methods was approximately 2.64 eV [53]. The slight increase observed in the band gap of thin film can be attributed to differences in the form of the material and the synthesis

procedures. Factors such as film thickness, substrate-induced strain, and the annealing process in the CBB thin film may contribute to shifts in localized excitons within the band gap.

Next, we analyze the recorded absorption and emission spectra of the CBB thin film, as shown in figure 1(c). A single prominent emission peak is observed in both cases, i.e. no additional peak associated with defect states is present in the spectra, indicating the high crystallinity of the sample and minimal structural defects. This observation also suggests that the absorption and recombination processes are dominated by intrinsic transitions rather than defect-related transitions. We find that the absorption spectrum peaks at 2.85 eV while the emission is centered at approximately 2.66 eV, consistent with a previous report of some us [35], with a tail up to 2.2 eV.

To further probe the charge dynamics of photoexcited carriers, we perform time-resolved PL (TRPL) measurements. The decay profile is well fitted by a multiexponential function, with an R^2 value of approximately 0.999. The average carrier lifetime is calculated to be 5.09 ns, as shown in figure 1(d). This short lifetime is characteristic of a direct band gap semiconductor and indicates efficient radiative recombination of photogenerated electron–hole pairs [65], further supporting the steady-state PL observation of a single emission peak. These findings strongly suggest the high optical quality of the CBB thin film and highlight its potential for optoelectronic applications where such properties are desirable [58].

Comparison with the absorption and emission spectra suggests that the red-shifted emission can be associated with the evolution of the exciton towards a self-trapping of charge carriers, in a fashion similar to other perovskites and perovskite-related materials [66–70]. In this regard, previous computational results suggest that electron polarons are stable in CBB, while holes do not localize [35, 49]. However, the strong Coulomb interaction in the excited state might bring to self-trapped excitons, in which both the charge carriers are localized [68, 71, 72]. We verify computationally that this is not the case for CBB, as we estimate an ephemeral stability for the self-trapped exciton, which is likely to be swiftly dissociated at room temperature (see section S2 of SI).

Overall, the experiment and these preliminary computational results suggest that the observed emission may be related with a hole from the valence band recombining with a small electron polaron [35]. This picture is also consistent with CBB being very efficient in transferring its holes to other semiconducting materials in heterojunctions, while the electrons need to migrate to the interface with liquid to catalyze heterogeneous redox reactions [35]. Therefore, we next focus on a detailed study of the energy levels of electron polarons in CBB as well as the associated electron mobility which are fundamental to understand the efficiency of this material for heterogeneous photocatalysis. This will be the subject of the following sections.

3. Structural and electronic properties of small electron polarons in CBB

We model bulk CBB using a tetragonal supercell ($a = 15.944$ Å, $b = 27.616$ Å, and $c = 19.374$ Å, corresponding to the experimental density [35, 73]). Starting from the neutral supercell at room temperature, as achieved from a previous simulation [35], we carry out a 9 ps molecular dynamics (MD) run for the system in which an additional electron is injected. We use the CP2K suite of programs [74–77] and carry out the calculations with a non-empirical hybrid-DFT functional, [78, 79] which has proven to accurately reproduce the electronic properties of CBB. (see [35] and section S3 of SI for thorough computational details).

By monitoring the time-dependent evolution of the highest singly occupied molecular orbital (SOMO) of the negatively charged system, we clearly observe a localized state in the band gap of the material, below the conduction band maximum (CBM). This is preserved throughout the MD simulation, see figure 2(a). The position of the SOMO energy level shows oscillation on a sub-picosecond timescale, while the cumulative average appears to be fairly converged in the considered time span (as also is the energy of the supercell, see figure S3). The electronic density of states (DOS) averaged over the entire MD trajectory (figure 2(b)) features a broad peak centered at 1.05±0.01 eV below the CBM of the material (error calculated via block analysis [80], see figure S4). The isodensity representation of the spin density (figure 2(c)) and the electron localization function (figure S5) reveal electron localization and thus polaron formation in a single $BiBr_6^{3-}$ unit, associated with local and sizable distortions (*vide infra*). Notwithstanding the large spread in the energy levels observed, evidenced by full width at half maximum of 1.01 eV, we note that no significant differences are observed in the extent of charge localization when sampling the spin density associated with structural configurations representing different positions in the distribution (see figure S6).

Having established the occurrence of a small polaron in CBB, we then investigate the nature of the local geometrical distortions for the polaron-bearing unit. In this regard, we note that we do not observe any hopping event during the MD simulation, i.e. the polaron remains on the same site in which it has

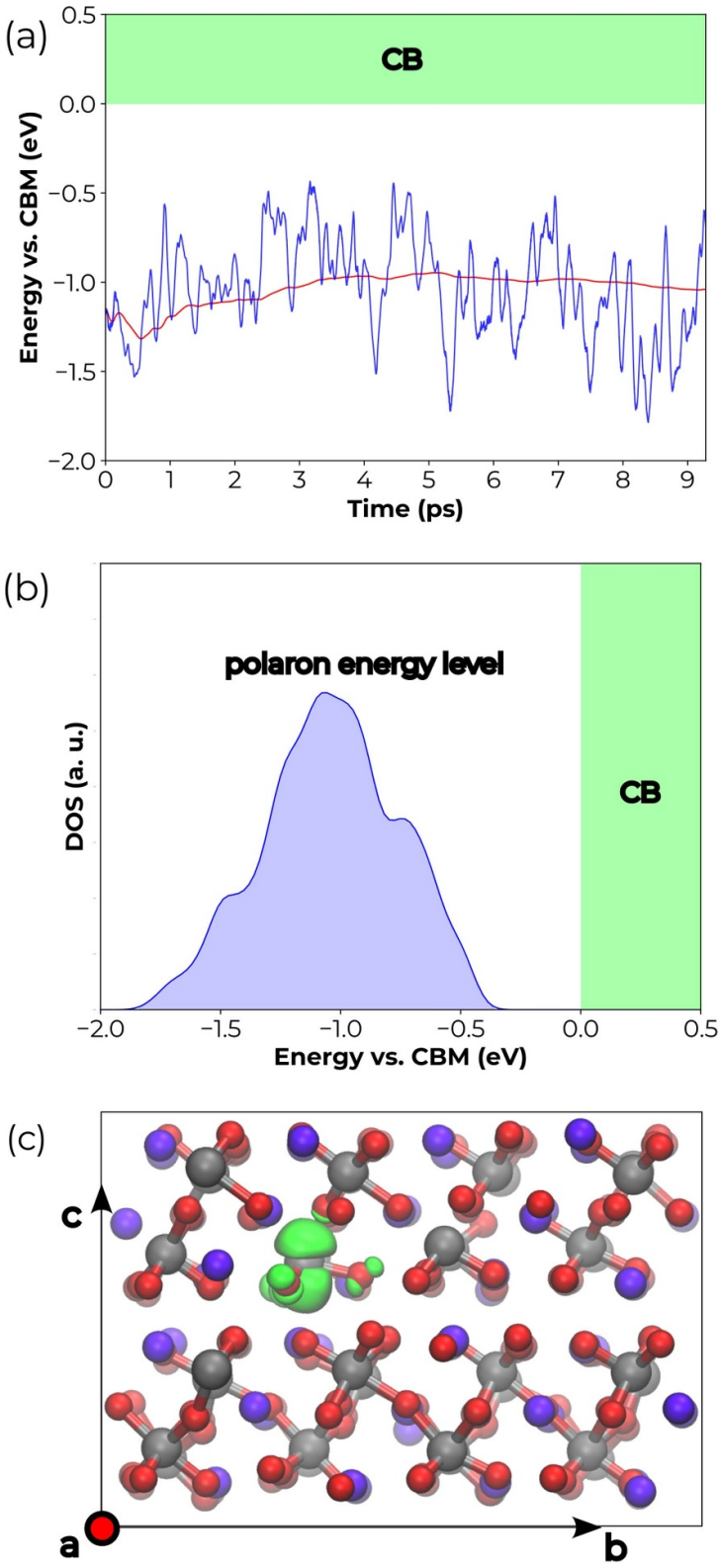

Figure 2. (a) Time-dependent evolution of the SOMO energy level of the CBB supercell with an extra electron, as calculated from MD simulation (blue curve) and cumulative average (red curve). (b) Electronic DOS averaged over the MD trajectory for the polaron energy level. All energy values are referred to the position of the CBM of the neutral system. (c) Isodensity representation of the spin density for the system bearing the polaron (isovalue: 0.001).

been primarily formed (see figures S7 and S8 showing that the polaronic distortion is retained on the same site throughout the MD trajectory). In figure 3(a), we report the distributions of Bi–Br distances for the polaronic Bi and for Bi ions in the neutral supercell, highlighting a clear difference. We observe two peaks for the pristine bulk, related to Bi–Br bonds involving single-bonded and bridging Br atoms

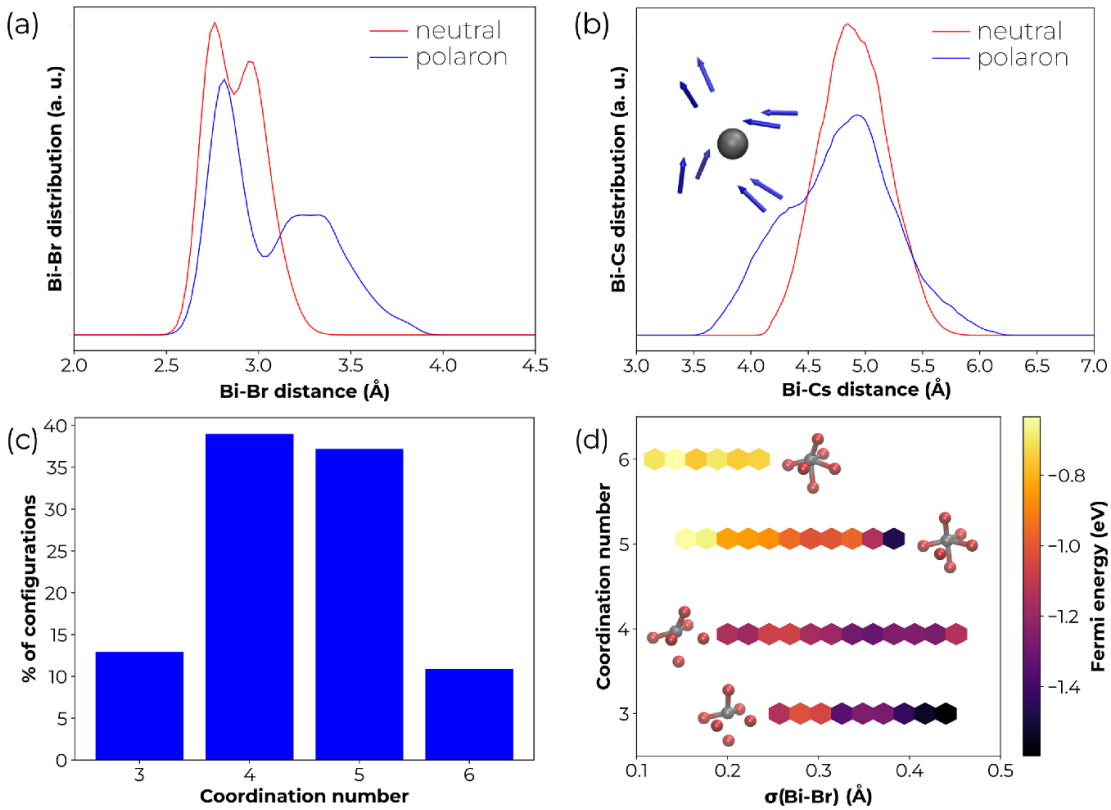

Figure 3. Distributions of (a) Bi–Br and (b) Bi–Cs distances for the Bi bearing the polaron (blue lines) against those of Bi in the neutral supercell (red lines). Inset of panel (b) provides a depictions of the displacements of Cs ions towards the polaron site. (c) Histogram showing the percentage of configuration with Br coordination numbers of three, four, five and six for the polaron. A cut-off radius of 3.3 Å is employed to define a coordinating Br (see main text). (d) Heat map of the polaron binding energy associated with different coordination numbers (three, four, five, and six, respectively) of the Bi bearing the polaron. For each, the binding energy is calculated vs. the standard deviation of Bi–Br distances.

in the octahedral unit, the former peaked at slightly longer distance than the latter (≈ 2.7 Å vs. ≈ 2.8 Å). At variance with this, Bi–Br distances for the polaron are found to shift towards higher values. In particular, the second peak is sensitively broadened, well beyond the value for Bi–Br bond lengths in the neutral material, thus suggesting one or multiple bonds being broken.

Next, we consider the distribution of Bi–Cs distances, given in figure 3(b). The polaron appears to exert a marked attraction on the surrounding Cs ions, as we observe the appearance of a shoulder at lower distances (up to ≈ 1 Å with respect to the neutral material). This phenomenon is connected with most of Cs ions being displaced from their position (see inset of figure 3(b)), in close resemblance to a solvent response, typically observed in solutions [81–83]. We can roughly determine the contributions of these motions to the global energy level of the polaron, by carrying out calculations on a subset of structural configurations in which we exchange the position of the Cs ions with the average ones from neutral MD simulation. Recalculation of the energy levels provides a difference of 0.19 eV, which can be estimated as the contribution of Cs ion displacement to the total polaron stabilization.

To further verify the connection between the calculated energy level and the local distortions, we analyze the coordination number of the Bi bearing the polaron, defined with a cut-off distance of 3.3 Å for Bi–Br bonds, i.e. beyond the threshold of the respective distribution. From the histogram in figure 3(c), we observe that, in contrast to the neutral bulk, for which each Bi has always six-fold coordination, the polaron site features a majority of four-fold (39.0%), five-fold (37.2%) and even three-fold (12.9%) coordination with only exiguous fractions of structural configurations displaying six (10.9%) coordinating Br ions. Then, we analyze the energetics in conjunction with the coordination number and the local distortion. For the latter, we consider the standard deviation of the distances between the Bi atom and six Br first neighbors. The heat-map presented in figure 3(d) evidences that less (more) coordinated and more (less) distorted structural configurations entail a higher (lower) stabilization of the polaron, thus justifying the observed broad peak in figure 2(b), which essentially stems from the soft nature of the CBB lattice. Such a result is also qualitatively consistent with the broad peak showing a pronounced tail, as observed in the emission spectrum.

Then, we calculate the polaron energy levels using the grand-canonical formulation of defects in crystalline semiconductors [84, 85], in which the formation energy of a defect X with charge q in the relaxed nuclear coordinates R_q is:

$$G_{\mathrm{f}}\left[X\left(R_q,q\right)\right]=G\left[X\left(R_q,q\right)\right]-G\left[\mathrm{bulk}\right]+\sum n_i\mu_i+q\left(\epsilon_{\mathrm{v}}+\mu_e\right)+E_{\mathrm{corr}}\left[X\left(R_q,q\right)\right]. \tag{2}$$

In equation (2), $G[\mathrm{bulk}]$ and ϵ_{v} are the free energy and the valence band maximum of the neutral bulk semiconductor, respectively; $G[X(R_q,q)]$ the free energy of the supercell bearing the defect with charge q, μ_i the chemical potential of the species i added/subtracted from the supercell n_i times, μ_e the chemical potential of the electron, and $E_{\mathrm{corr}}[X(R_q,q)]$ a correction term which cleanse the DFT total energy of charged supercell from the spurious electrostatic interactions among periodic replicas (see section S3 of SI and [84, 85] for details on the correction scheme).

We can describe the process of electron polaron formation in a defect-less material via the following half-reaction:

$$CBB+e^{-}\rightarrow pol(-). \tag{3}$$

It follows that the adiabatic energy level associated with the $(-1/0)$ charge transition level reads as: [86]

$$\mu_{\mathrm{ad}}\left(-/0\right)=G\left[\mathrm{pol}\left(R_{-1},-1\right)\right]+E_{\mathrm{corr}}\left[\mathrm{pol}\left(R_{-1},-1\right)\right]-G\left[\mathrm{bulk}\right]-\epsilon_{\mathrm{v}}, \tag{4}$$

where $G[\mathrm{pol}(R_{-1},-1)]$ is the free energy of the supercell with the electron polaron and $E_{\mathrm{corr}}[\mathrm{pol}(R_{-1},-1)]$ the finite-size correction associated with it. The free-energy difference appearing in equation (4) is calculated from MD simulations using the thermodynamic integration technique, by which we evaluate this equilibrium property from the energy differences related with vertical transitions for the pristine bulk, the polaronic system, and fictitious systems connecting them via the following Hamiltonian $\mathcal{H}_\eta$ as: [87]

$$\mathcal{H}_\eta=\eta\mathcal{H}_{\mathrm{pol}}+\left(1-\eta\right)\mathcal{H}_{\mathrm{pristine}}, \tag{5}$$

that allows mixing those of the reactants and the products via the Kirkwood coupling parameter $0\leqslant\eta\leqslant1$ [87]. From equation (5), it is possible to perform MD simulations for different values of η, obtaining the respective trajectories R_η. Then, for each R_η, we can calculate the average vertical energy difference associated with injection/removal of an electron: [88, 89]

$$\langle\Delta E\rangle_\eta=E[(R_\eta,-1)]-E\left(R_\eta,0\right)]. \tag{6}$$

Integration of these vertical energy gaps over η provides us with the free-energy estimate:

$$G\left[\mathrm{pol}\left(R_{-1},-1\right)\right]-G\left[\mathrm{bulk}\right]=\int_0^1\langle\Delta E\rangle_\eta\,\mathrm{d}\eta \tag{7}$$

We here use a three-point approximation ($\eta=0,\ 0.5,\ 1$) to evaluate the thermodynamic integral, as it offers a good balance between accuracy and computational efficiency [90, 91]. $\langle\Delta E\rangle_0$ and $\langle\Delta E\rangle_1$ correspond to vertical injection of an electron onto the pristine CBB and to vertical ionization of the polaron, respectively. While the former represents the sampling of the semilocalized conduction band edge, the latter gives the vertical detachment energy of the polaron, which reads as:

$$\mu_{\mathrm{ver}}\left(-/0\right)=\langle\Delta E\rangle_{R_{-1}}+E_{\mathrm{corr}}\left[\mathrm{pol}\left(R_{-1},0\right)\right]-E_{\mathrm{corr}}\left[\mathrm{pol}\left(R_{-1},-1\right)\right]-\epsilon_{\mathrm{v}}, \tag{8}$$

where $E_{\mathrm{corr}}[\mathrm{pol}(R_{-1},0)]$ is a correction term necessary to get rid of the ionic polarization charge, remaining in the neutral supercell after vertical removal of the electron from the system bearing the polaron (see section S3 of SI and [92]). Finally, the adiabatic and vertical polaron binding energies, i.e. the energy gains upon localization of the electron with respect to the semilocalized conduction band edge (ϵ_{c}) are:

$$E_{\mathrm{b}}^{\mathrm{ad}}\left[\mathrm{pol}\left(-\right)\right]=\epsilon_{\mathrm{c}}-\mu_{\mathrm{ad}}\left(-/0\right), \tag{9}$$

$$E_{\mathrm{b}}^{\mathrm{ver}}\left[\mathrm{pol}\left(-\right)\right]=\epsilon_{\mathrm{c}}-\mu_{\mathrm{ver}}\left(-/0\right), \tag{10}$$

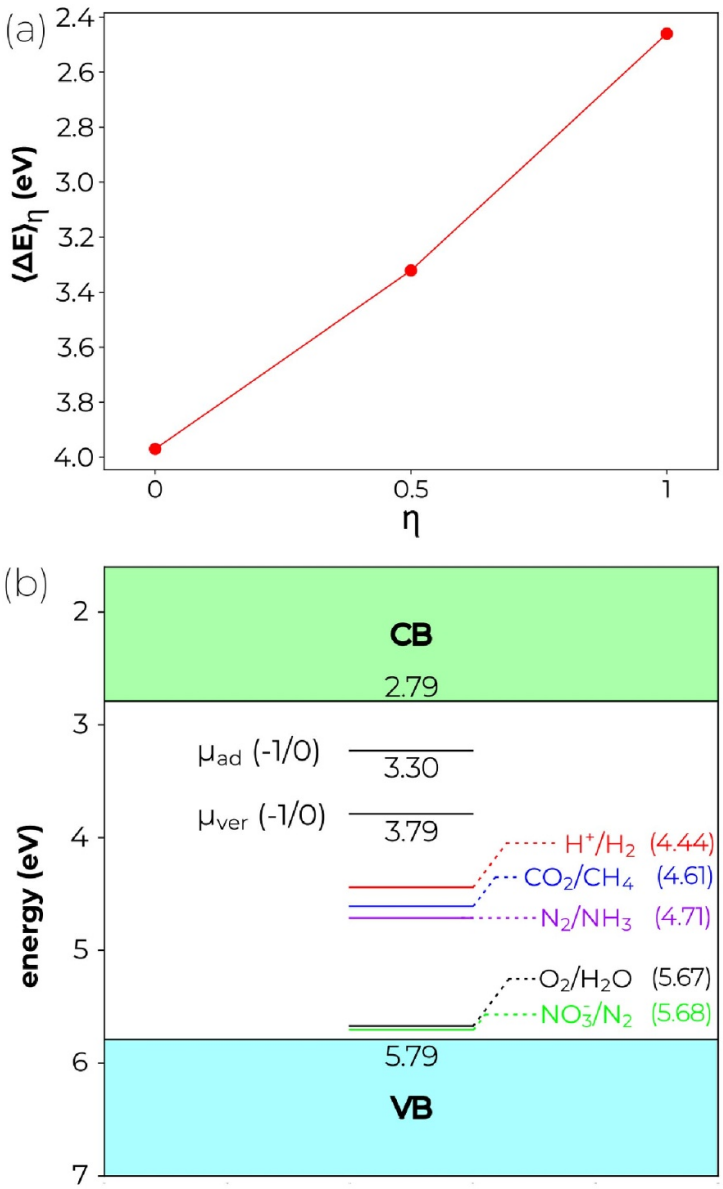

Figure 4. (a) Average vertical energy gaps between reduced and oxidized system, $\langle \Delta E \rangle_\eta$, as a function of the Kirkwood coupling parameter η. Values are referred with respect to the vacuum level. (b) Schematic representation of the band alignment for CBB [35], including the adiabatic and vertical charge transition levels of the electron polaron and redox potentials of interest for photocatalysis.

The calculated quantities, referred with respect to the band edges of CBB, are then expressed against a physical reference, employing the band alignment from [35], which places the valence band maximum (VBM) and CBM of the perovskite at 5.79 and 2.79 eV below the vacuum level, respectively, see. figure 4(b). Hence, our calculated $\mu_{ad}(-/0)$ and $\mu_{ver}(-/0)$ are found to lie at 3.30 and 3.79 eV below the vacuum level, implying polaron binding energies of 0.49 and 1 eV, respectively. The adiabatic value is 0.11 eV smaller than that calculated at 0 K [35], suggesting that thermal motions slightly destabilize polaronic localization. The position of the polaronic energy levels is consistent with the interpretation of the emission spectrum measured for the thin film, i.e. radiative recombination between the electron polaron and a hole from the VBM. For instance, we also perform time-dependent DFT [93, 94] calculations (see section S3 of SI for details) on a charge-neutral supercell bearing the polaronic distortion, in order to evaluate the energetics associated with the emission process, which we ascribe to recombination of a VBM hole and an electron polaron. Our simulated spectrum, see figure S9, presents a peak at ≈2.7 eV, in fair agreement with the experiment, thus confirming the robustness of the proposed physical picture.

We note that the polaron energy levels are favorably aligned with respect to redox potentials associated with H_2 generation, CO_2 reduction (4.61 eV vs. vacuum), and N_2 fixation (4.71 eV vs. vacuum)

[95]. This suggests that CBB could be potentially employed in a variety of photocatalytic processes and that the reaction mechanism is likely to be mediated by polarons at the water-semiconductor interface. Furthermore, CBB might also work as photoanode, due to the adequate alignment of its VBM with commonly studied oxidation processes in heterogeneous photocatalysis, such as the water photo-oxidation (5.67 eV vs. vacuum) and denitrification of nitrate to N_2 (5.68 eV vs. vacuum) [95]. We pinpoint that charge carriers should be able to migrate toward the relevant surface for the reaction to take place. However, the occurrence of small polarons in the *bulk* suggests that photocatalytic activity might be jeopardized by the limited mobility of photogenerated charge carriers, when also considering their lifetime on the nanosecond time scale.

4. Migration of small electron polarons in CBB

Polaron dynamics is here modeled considering a two-state model [96]. Within this approach, the initial and final states, A and B, corresponding to charge localization on two different sites, are connected, along a generalized coordinate Q, by a transition state (TS), see figure 5(a). Under the harmonic approximation, diabatic potential energy surfaces associated with states A and B exhibit quadratic dependence on the reaction coordinate Q, intersecting each other at the TS [97]. Within the limit of rapid nuclear motion, the polaron remains localized on its initial site rather than following the adiabatic minimum energy path (diabatic limit); conversely, when nuclear dynamics is slower than the electronic one (i.e. at the adiabatic limit), the system follows the ground-state surface [98, 99]. Given the matrix representation of the Hamiltonian for the considered two-state model: [100]

$$H = \begin{bmatrix} \epsilon_{\mathrm{A}} & J \\ J & \epsilon_{\mathrm{B}} \end{bmatrix}, \tag{11}$$

where ϵ_{A} and ϵ_{B} are the single-particle energy levels of the polaron state and J is the coupling strength between them, the adiabatic states, E_2 and E_1, are described by the eigenvalues and eigenvectors of the Hamiltonian.

To assess the kinetics of polaron hopping, we adopt the Marcus–Emin–Holstein–Austin–Mott theory, for which the rate of electron transfer from a polaron site to another is defined as: [101–105]

$$k_{\mathrm{ET}} = \kappa \nu \Gamma e^{-\frac{E_{\mathrm{a}}}{k_{\mathrm{B}} T}}. \tag{12}$$

In equation (12), κ is the electronic transmission coefficient, ν the phonon frequency associated to the hopping process, Γ the nuclear tunneling factor, E_a the activation energy required to allow polaron migration, k_{B} the Boltzmann constant and T the absolute temperature. Since nuclear quantum tunneling is relevant at low temperatures and only for light elements [106], Γ is assumed equal to unity, similarly to previous work [106, 107]. κ is evaluated according to the following relation [108]:

$$\kappa = \frac{2P}{1+P} \tag{13}$$

in which P measures the probability of remaining on the low-energy branch of the adiabatic energy surface after moving toward the TS [108]:

$$P = 1 - \exp\left[-\frac{\pi^2 J^2}{h\nu\sqrt{4\pi\,(E_{\mathrm{a}} + J)\,k_B T}}\right]. \tag{14}$$

The activation energy for the hopping path, E_{a}, is calculated as:

$$E_{\mathrm{a}} = E(\mathrm{TS}) - E(\mathrm{pol}), \tag{15}$$

i.e. the total-energy difference between the TS and the ground-state polaron, see the adiabatic energy surface in figure 5(a). The minimum energy pathways toward the TS are here explored via the nudged elastic band method (NEB), [109] which allows to connect the initial and final states through a discrete number of images of the system (see section S3 of SI for Computational Details). The electronic coupling strength J, see figure 5(a), is estimated as: [100]

$$J = \frac{1}{2}\left[\epsilon_{\mathrm{SUMO}}(\mathrm{TS}) - \epsilon_{\mathrm{SOMO}}(\mathrm{TS})\right], \tag{16}$$

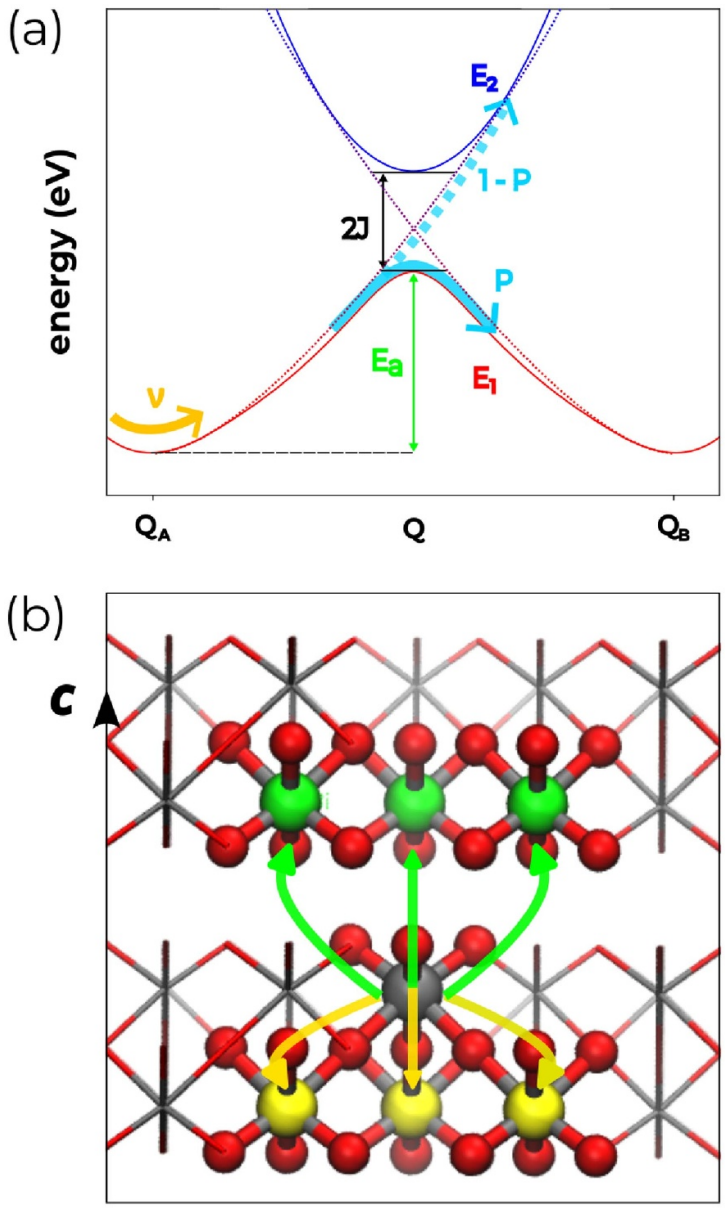

Figure 5. (a) Energy profile for polaron migration showing diabatic (dashed lines) and adiabatic (red and blue solid lines) energy surfaces, E_1 and E_2, vs. the configurational coordinate Q (see main text). ν (yellow solid arrow) is the attempt frequency, P (pale blue solid arrow) the transition probability of remaining in the low-energy state, $1 - P$ (dashed pale blue arrow) the transition probability of moving to the high-energy state, E_a the activation energy for the polaron migration, J the coupling strength between the single-particle energy levels of the polaron state. (b) Schematic representation of the nearest neighbors of a Bi atom within the same layer (intralayer, yellow atoms) and on an adjacent layer (interlayer, green atoms). The corresponding arrows represent the polaron hopping pathways considered in the following analysis, namely intralayer and interlayer polaron diffusion. Cs ions are not shown for better clarity of representation.

where $\epsilon_{\mathrm{SOMO}}(\mathrm{TS})$ and $\epsilon_{\mathrm{SUMO}}(\mathrm{TS})$ are the single-particle energy levels for the highest singly occupied (SOMO) and lowest singly unoccupied molecular orbitals (SUMOs), as calculated at the TS [110].

The phonon frequency involved in the hopping process can be approximated by a one-dimensional effective frequency [111, 112], within the limit of the high temperature regime ($h\nu \ll k_{\mathrm{B}}T$) [106]. It is evaluated as the second derivative of E vs. Q referring to the initial state $Q(A)$:

$$\nu_{\mathrm{eff}} = \sqrt{\frac{\partial^2 E}{\partial Q^2}} \tag{17}$$

with $Q(n)$ being nth configurational coordinate defined as:

$$Q(n)^2 = \sum_i m_i \left|\mathbf{r}(n)_i - \mathbf{r}(\mathrm{A})_i\right|^2 \tag{18}$$

Table 1. Calculated parameters associated with polaron hopping. d (given in Å) is the distance between Bi atoms involved in the hopping process, while ΔQ is the mass-weighted distance between the initial and final states [given in Å $\cdot(amu)^{1/2}$]. All energies (E_a, $h\nu_{eff}$, J, see main text) are given in meV, kinetic constants are given in s^{-1} units.

path	d	ΔQ	E_a	$h\nu_{eff}$	J	κ	k_{ET}
intralayer	5.97	17.7	238	22.1	497	1.0	$1.39\cdot10^{9}$
interlayer	7.61	16.3	434	25.2	275	1.0	$3.11\cdot10^{5}$

where n is the ordinal number of each NEB image, m_i and $\mathbf{r}_i$ the mass and the position of the ith atom involved in the transition. We here note that the calculated mass-weighted coordinate distance between the initial and final states (i.e. $\Delta Q = Q(B) - Q(A)$) is large (>10 Å $\cdot(amu)^{1/2}$ for all the considered cases, *vide infra* and table 1), thus implying that large nuclear motions are required for the electron to be displaced from one site to another in a physical picture which is fully consistent with semi-classical polaron hopping [81].

The layered arrangement of CBB gives rise to two distinct types of nearest neighbors for each bismuth cation (three intralayer and three interlayer), as illustrated in figure 5(b). Therefore, the presented methodology is here applied to determine rates for both hopping sites. The results of NEB calculations are presented in figure 6 and S10, for intralayer and interlayer hopping, respectively. The calculated data, necessary to estimate the kinetics of polaron hopping, and the respective rates are collected in table 1. Our results denote glaring differences in intralayer and interlayer pathways, in terms of activation energies (0.238 vs 0.434 eV) and coupling strengths (0.497 vs 0.275 eV) (see panels (b) and (c) of figures 6 and S9). These results clearly impact the calculated electron transfer rate constants: the intralayer path displays $k_{ET} = 1.39\cdot10^{9}$ s^{-1} to be compared with the value of $3.11\cdot10^{5}$ s^{-1}, thus showing a sizable difference of almost four orders of magnitude. This can be interpreted in terms of the different hopping distances (5.97 vs 7.61 Å) and the distinct environments accompanying the process. In fact, the electronic distributions of the TSs corresponding to the two pathways show marked differences: in particular, the intralayer one exhibits delocalization across both Bi sites involved in the hopping process, while the other still entails a high degree of localization on the initial Bi site, see figures 6(a) and S10.

Next, we evaluate electron mobility, μ, by performing random hopping simulations that are evolved in the CBB lattice, via the kinetic Monte Carlo (kMC) stochastic algorithm [113], which is often employed to model diffusion of localized charges within a semiconductor [106, 107, 114, 115]. In this scheme, the lattice is represented as an ideal network of hopping sites, connected by transitions whose probability is governed by Arrhenius-like rate constants, derived from the Marcus-Emin-Holstein theory described above. Each kMC trajectory evolves by probabilistically selecting hopping events according to their rates, and the mean squared displacement $\langle L(t)^2\rangle$ is monitored as a function of time until the diffusive regime is reached [116]. As a result of multiple kMC runs, the diffusion coefficient, D, can be evaluated from the slope of the $\langle L(t)^2\rangle$ vs. t curve, i.e. formally from equation:

$$D = \lim_{t\to\infty} \frac{\langle L(t)^2\rangle}{2Nt}, \tag{19}$$

where $\langle L(t)^2\rangle$ is the mean squared displacement and N is the dimensionality of the system. Electron mobility is finally calculated according to the Einstein–Smoluchowski equation [117]:

$$\mu = \frac{eD}{k_b T}, \tag{20}$$

where e is the electron charge.

Averaging over 20 000 independent trajectories yields an average electron mobility of $4.57\cdot10^{-5}cm^2V^{-1}s^{-1}$, which falls within the typical range for materials whose transport is dominated by small polaron hopping, e.g. $BiVO_4$ ($1.38\cdot10^{-4}cm^2V^{-1}s^{-1}$) [106], $NaTaO_3$ and $KTaO_3$ ($1.87\cdot10^{-4}$ and $2.94\cdot10^{-6}cm^2V^{-1}s^{-1}$) [118]. Beyond the absolute value, our analysis evidences a pronounced anisotropy in polaron transport: while in-plane mobility (on the ab plane) is $3.23\cdot10^{-5}cm^2V^{-1}s^{-1}$, out-of-plane mobility along the stacking direction is more than two orders of magnitude smaller ($3.08\cdot10^{-7}cm^2V^{-1}s^{-1}$). Such a strong anisotropy can be rationalized in terms of the substantial differences in the energetics for the corresponding interlayer and intralayer hopping paths.

The combination of low mobility and strong anisotropy has important implications for photocatalysis, allowing to explain the loading-dependent performance of CCB-based heterojunctions, which usually see a dramatic drop in photoconversion efficiency, after reaching a certain threshold in the device composition. [35, 49, 51] In fact, on the basis of our results it is expected that large CBB domains or

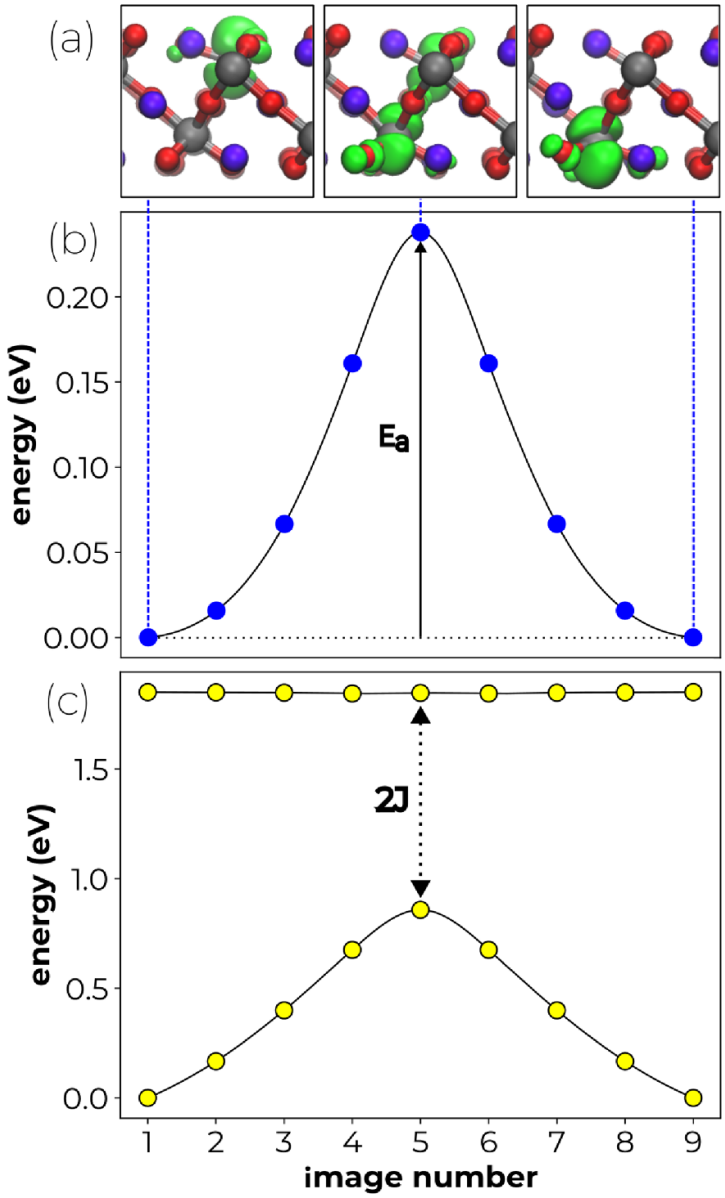

Figure 6. (a) Isodensity representation of the spin density (isovalue 0.001) for the initial, transition, and final state for intralayer NN polaron hopping, as calculated from the NEB trajectory. (b) Total-energy profile of polaron hopping along the NEB path composed of seven images between two intralayer first neighbors. Energies are referred to that of the initial state. (c) Kohh-Sham energy levels of the highest SOMO and lowest SUMO along the polaron migration path. Energies are referred to that of the SOMO in the initial state.

excessive thickness along the stacking direction should be avoided, because electrons generated deep within the bulk are unlikely to migrate across multiple layers before recombining, despite the extended lifetimes that may be provided by heterojunction architectures separating holes and electrons. These constraints suggest practical design rules, such as favor 2D morphologies and few-layer stacks to shorten the interlayer path and use of conductive/2D scaffolds to further promote charge separation [119]. Another option is represented by engineering effective organic spacers among the layers to boost out-of-plane hopping, as attempted in other 2D layered perovskites [120]. In fact, the issue of transport anisotropy has been observed also for Ruddlesden–Popper perovskites, in which insulating organic species act as quantum wells and create barriers that suppress out-of-plane carrier transport while maintaining relatively high in-plane mobility [121].

Finally, we comment on possible modifications of the proposed physical picture, which may be induced by defect chemistry and doping. For the former, we note that electrons, in principle, could cross layers via intercalating defects. In particular, interlayer Bi interstitials are suggested to be among the most abundant defects under Bi-rich conditions [58]. Bearing this in mind, we model the intercalating Bi defect in the 3+ charge state, Bi_{ic}^{3+} and then consider the possible localization of a single electron

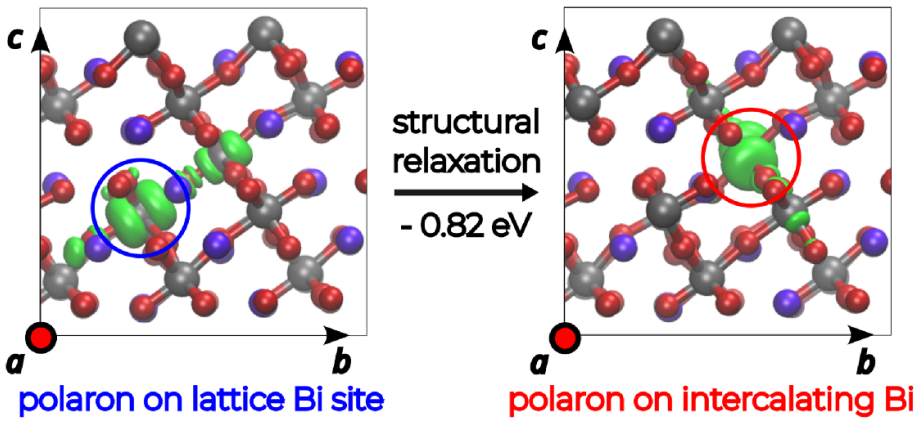

Figure 7. Isodensity representation of the spin density (isovalue 0.001) before (left panel) and after full relaxation (right panel), showing shift in the localization of the extra electron from a lattice site to an intercalating Bi. The sites are highlighted with blue and red circles, respectively. The energy gain upon relaxation is also reported.

on it, i.e. Bi_{ic}^{2+}. In particular, we aim at estimating the relative stability of trapping on Bi_{ic} with respect to polaron formation on lattice Bi. To this end, we perform a structural relaxation of a supercell including an intercalating Bi *and* a polaron-bearing site close to it. First, we relax the system keeping the coordinates of the polaronic site fixed, thus preserving charge localization on it, see figure 7, even if some protrusion towards the interstitial is already observed. Upon full structural relaxation, we observe immediate disruption of the polaronic distortions on the lattice site and charge localization on the intercalating Bi, which is accompanied by a substantial energy gain of 0.82 eV, see figure 7. Therefore, our calculations indicate that intercalating Bi atoms may even worsen the charge transport properties of CBB, as they tend to form trap states, which are stabler than polaronic localization on a regular lattice site. This result is in line with previous studies on affine materials, suggesting that layered perovskites might not be as defect-tolerant as their three-dimensional counterparts [48]. It also suggests that Bi-rich conditions should be avoided in the preparation of CBB and stoichiometric conditions, such as those employed here, should be preferred.

Concerning doping, this might be a more feasible option to boost the interlayer mobility in CBB. However, so far, intercalation of dopants has been successful in augmenting light-emission via formation of strong interlayer excitons (e.g. Ag doping in [58]), thus representing a material engineering strategy more suitable for photo-emitting devices rather than photocatalytic applications. Nevertheless, the literature on the subject is still rather scarce and, therefore, it represents surely a future research direction to be explored.

5. Conclusions

In summary, we studied the electronic properties of CBB, with a particular focus on electron polaron formation and migration. First, spectroscopic measurements indicated that the light-induced excitation evolves towards a self-trapped exciton, suggesting localization of charge carriers. Indeed, by performing advanced hybrid-DFT calculations and MD simulations, we have shown that photogenerated electrons form small polarons, a process driven by substantial structural reorganization involving both the inorganic sublattice and A-site cations. The electron polaron was found to lie 0.6 eV below the conduction band edge, in agreement with emission spectra and in favorable alignment with redox potentials relevant for photocatalytic reduction processes such as H_2 evolution.

We then evaluated electron transport across the material, combining the definition of hopping rates in the framework of Marcus–Emin–Holstein–Austin–Mott theory with kinetic Monte Carlo simulations. Polaron mobility was found to be highly anisotropic. In particular, since intralayer transport is comparatively slow, excessive growth in the out-of-plane direction (i.e. stacking of many layers) is expected to hinder charge extraction, highlighting the need to control thickness to ensure that photogenerated electrons can reach the relevant interfaces. Furthermore, intercalating defects, such as interstitial Bi, seem to have a detrimental impact on mobility as they tend to form deep traps, in line with what has been recently observed for dopants. Overall, the present results indicate that the photocatalytic performance of CBB will strongly depend on growth conditions, morphology, particle size, and loading, as well as on

the use of heterojunction architectures that spatially separate electrons and holes. Such design considerations appear to be essential to minimize recombination losses and to efficiently exploit the potential of CBB for photocatalysis.

Data availability statement

The data that support the findings of this study are openly available at the following URL/DOI: https://github.com/Michi12Michi/CBB-Supporting-data.

Supplementary data available at https://doi.org/10.1088/2515-7655/ae2159/data1.

Acknowledgment

F A, M L, and S C thankfully acknowledge PRIN 2022-PNRR Grant (P2022W9773) for funding. S C also acknowledges the PRIN 2022 project INTERFACE (2022HWWW3S). Andrea Listorti acknowledges the PRIN2022 project REVOLUTION, (2022HRZH7P) and PRIN 2022-PNRR Grant BEAGLE (P20223HSWX). Alessandro Landi gratefully acknowledges PRIN 2022 Grant 2022XSC9P5 (INTESA-SOLE) by Ministero of Universitá e Ricerca (MIUR) for funding. F A and M L also acknowledge the CINECA award under the ISCRA initiative, for the availability of high-performance computing resources: project MHP-DEF. J W acknowledges funding from the Swedish Strategic Research Foundation through a Future Research Leader programme (FFL21-0129), the Swedish Research Council (2019-03993), European Research Council (ERC Starting Grant no. 101162195), and the Knut and Alice Wallenberg Foundation (Nos. 2023.0032 and 2024.0042).

We thank Giorgio Palermo for useful discussions.

Associated content

Experimental Methods, Computational details and supplementary figures are provided in the Electronic Supplementary Information. All the relevant data (inputs, MD outputs) used to produce the computational results presented in this work are available at the following public repository: https://github.com/Michi12Michi/CBB-Supporting-data

Author contributions

Michele Loriso 0009-0000-5958-1768
Data curation (lead), Formal analysis (lead), Investigation (equal), Methodology (equal), Visualization (lead), Writing – original draft (lead)

Sohail Azmat 0000-0003-1405-2357
Data curation (supporting), Formal analysis (supporting), Investigation (supporting), Methodology (supporting), Visualization (supporting), Writing – original draft (supporting)

Andrea Listorti 0000-0001-5436-4895
Data curation (supporting), Formal analysis (supporting), Funding acquisition (supporting), Investigation (supporting), Resources (supporting), Writing – review & editing (supporting)

Alessandro Landi 0000-0003-3627-5535
Data curation (supporting), Formal analysis (supporting), Investigation (supporting), Methodology (supporting), Supervision (supporting), Visualization (supporting), Writing – review & editing (supporting)

Julia Wiktor 0000-0003-3395-1104
Formal analysis (supporting), Methodology (supporting), Validation (equal), Writing – original draft (supporting), Writing – review & editing (supporting)

Filippo De Angelis 0000-0003-3833-1975
Conceptualization (supporting), Formal analysis (supporting), Funding acquisition (supporting), Methodology (supporting), Project administration (supporting), Resources (supporting), Supervision (supporting), Validation (equal), Writing – review & editing (supporting)

Andrea Peluso 0000-0002-6140-9825
Investigation (supporting), Methodology (supporting), Project administration (supporting), Supervision (supporting), Validation (equal), Writing – review & editing (supporting)

Silvia Colella 0000-0001-9704-8892
Conceptualization (supporting), Formal analysis (supporting), Funding acquisition (supporting), Investigation (supporting), Methodology (supporting), Resources (supporting), Supervision (supporting), Writing – original draft (supporting), Writing – review & editing (supporting)

Francesco Ambrosio 0000-0002-6388-9586
Conceptualization (lead), Data curation (supporting), Formal analysis (equal), Funding acquisition (lead), Investigation (equal), Methodology (equal), Project administration (lead), Resources (lead), Supervision (lead), Validation (equal), Writing – original draft (supporting), Writing – review & editing (lead)

References

[1] Tilsted J P, Bauer F, Deere Birkbeck C, Skovgaard J and Rootzén J 2023 Ending fossil-based growth: confronting the political economy of petrochemical plastics *One Earth* **6** 607–19
[2] Soeder D J 2025 *Energy Futures: The Story of Fossil Fuel, Greenhouse Gas and Climate Change* (Springer) pp 143–83
[3] Tachibana Y, Vayssieres L and Durrant J R 2012 Artificial photosynthesis for solar water-splitting *Nat. Photon.* **6** 511–8
[4] Ahmad H, Kamarudin S, Minggu L and Kassim M 2015 Hydrogen from photo-catalytic water splitting process: a review *Renew. Sustain. Energy Rev.* **43** 599–610
[5] Zou X and Zhang Y 2015 Noble metal-free hydrogen evolution catalysts for water splitting *Chem. Soc. Rev.* **44** 5148–80
[6] Chakravorty A and Roy S 2024 A review of photocatalysis, basic principles, processes and materials *Sustain. Chem. Environ.* **8** 100155
[7] Leng W, Barnes P R, Juozapavicius M, O'Regan B C and Durrant J R 2010 Electron diffusion length in mesoporous nanocrystalline TiO_2 photoelectrodes during water oxidation *J. Phys. Chem. Lett.* **1** 967–72
[8] Li X, Dai Y, Li M, Wei W and Huang B 2015 Stable Si-based pentagonal monolayers: high carrier mobilities and applications in photocatalytic water splitting *J. Mater. Chem. A* **3** 24055–63
[9] Fumanal M, Ortega-Guerrero A, Jablonka K M, Smit B and Tavernelli I 2020 Charge separation and charge carrier mobility in photocatalytic metal-organic frameworks *Adv. Funct. Mater.* **30** 2003792
[10] Wu Y, Chan M K Y and Ceder G 2011 Prediction of semiconductor band edge positions in aqueous environments from first principles *Phys. Rev. B* **83** 235301
[11] Guo Z, Ambrosio F, Chen W, Gono P and Pasquarello A 2018 Alignment of Redox levels at semiconductor–water interfaces *Chem. Mater.* **30** 94–111
[12] Ambrosio F, Wiktor J and Pasquarello A 2018 pH-dependent catalytic reaction pathway for water splitting at the $BiVO_4$–water interface from the band alignment *ACS Energy Lett.* **3** 829–34
[13] Guo Z, Ambrosio F and Pasquarello A 2020 Evaluation of photocatalysts for water splitting through combined analysis of surface coverage and energy-level alignment *ACS Catal.* **10** 13186–95
[14] Zhao Y, Gao J, Bian X, Tang H and Zhang T 2024 From the perspective of experimental practice: high-throughput computational screening in photocatalysis *Green Energy Environ.* **9** 1–6
[15] Ambrosio F, Wiktor J and Pasquarello A 2018 pH-dependent surface chemistry from first principles: application to the $BiVO_4$(010)–water interface *ACS Appl. Mater. Interfaces* **10** 10011–21
[16] Wen B, Andrade M F C, Liu L-M and Selloni A 2023 Water dissociation at the water-rutile TiO_2(110) interface from *ab initio*-based deep neural network simulations *Proc. Natl Acad. Sci.* **120** e2212250120
[17] Mai H, Le T C, Chen D, Winkler D A and Caruso R A 2022 Machine learning for electrocatalyst and photocatalyst design and discovery *Chem. Rev.* **122** 13478–515
[18] Sharma R K, Jena M K, Minhas H and Pathak B 2024 Machine-learning-assisted screening of nanocluster electrocatalysts: mapping and reshaping the activity volcano for the oxygen reduction reaction *CS Appl. Mater. Interfaces* **16** 63589–601
[19] Fajín J L C, Halder A K and Cordeiro M N D S 2025 Machine learning-guided prediction of activation energies for catalyst design in the water gas shift reaction *J. Phys. Chem. C* **129** 5353–60
[20] Etgar L, Gao P, Xue Z, Peng Q, Chandiran A K, Liu B, Nazeeruddin M K and Grätzel M 2012 Mesoscopic $CH_3NH_3PbI_3/TiO_2$ heterojunction solar cells *J. Am. Chem. Soc.* **134** 17396–9
[21] Burschka J, Pellet N, Moon S-J, Humphry-Baker R, Gao P, Nazeeruddin M K and Grätzel M 2013 Sequential deposition as a route to high-performance perovskite-sensitized solar cells *Nature* **499** 316–9
[22] Brenner T M, Egger D A, Kronik L, Hodes G and Cahen D 2016 Hybrid organic–norganic perovskites: low-cost semiconductors with intriguing charge-transport properties *Nat. Rev. Mater.* **1** 1–16
[23] Green M, Dunlop E, Hohl-Ebinger J, Yoshita M, Kopidakis N and Hao X 2021 Solar cell efficiency tables (version 57) *Prog. Photovolt., Res. Appl.* **29** 3–15
[24] Bisquert J and Juarez-Perez E J 2019 The causes of degradation of perovskite solar cells *J. Phys. Chem. Lett.* **10** 5889–91
[25] Zheng C and Rubel O 2019 Unraveling the water degradation mechanism of $CH_3NH_3PbI_3$ *J. Phys. Chem. Lett.* **123** 19385–94
[26] Mosconi E, Azpiroz J M and De Angelis F 2015 Ab Initio molecular dynamics simulations of methylammonium lead iodide perovskite degradation by water *Chem. Mater.* **27** 4885–92
[27] Hadi M, Islam M N and Podder J 2022 Indirect to direct band gap transition through order to disorder transformation of Cs 2 AgBiBr 6 via creating antisite defects for optoelectronic and photovoltaic applications *RSC Adv.* **12** 15461–9
[28] Ma Y and Zhao Q 2022 A strategic review on processing routes towards scalable fabrication of perovskite solar cells *Energy Chem.* **64** 538–60
[29] Zhu P, Chen C, Dai J, Zhang Y, Mao R, Chen S, Huang J and Zhu J 2024 Toward the commercialization of perovskite solar modules *Adv. Mater.* **36** 2307357
[30] Motti S G, Meggiolaro D, Martani S, Sorrentino R, Barker A J, De Angelis F and Petrozza A 2019 Defect activity in metal-halide perovskites *Adv. Mater.* **31** 1901183
[31] Ambrosio F, Mosconi E, Alasmari A A, Alasmary F A, Meggiolaro D and De Angelis F 2020 Formation of color centers in lead iodide perovskites: self-trapping and defects in the bulk and surfaces *Chem. Mater.* **32** 6916–24

[32] Huang H, Pradhan B, Hofkens J, Roeffaers M B J and Steele J A 2020 Solar-driven metal halide perovskite photocatalysis: design, stability and performance *ACS Energy Lett.* **5** 1107

[33] Wang J, Liu J, Du Z and Li Z 2021 Recent advances in metal halide perovskite photocatalysts: Properties, synthesis and applications *J. Energy Chem.* **54** 770–85

[34] Armenise V, Colella S, Fracassi F and Listorti A 2021 Lead-free metal halide perovskites for hydrogen evolution from aqueous solutions *Nanomaterials* **11** 433

[35] Romani L *et al* 2021 Experimental strategy and mechanistic view to boost the photocatalytic activity of $Cs_3Bi_2Br_9$ lead-free perovskite derivative by g-C_3N_4 composite engineering *Adv. Funct. Mater.* **31** 2104428

[36] Romani L *et al* 2021 Water-stable $DMASnBr_3$ lead-free perovskite for effective solar-driven photocatalysis *Angew. Chem. Int. Ed.* **60** 3611–8

[37] Tang Y *et al* 2022 Lead-free hybrid perovskite photocatalysts: surface engineering, charge-carrier behaviors and solar-driven applications *J. Mater. Chem. A* **10** 12296–316

[38] Romani L *et al* 2023 Air- and water-stable and photocatalytically active germanium-based 2D perovskites by organic spacer engineering *Cell Rep. Phys. Sci.* **4** 101214

[39] Chen S, Yin H, Liu P, Wang Y and Zhao H 2023 Stabilization and performance enhancement strategies for halide perovskite photocatalysts *Adv. Mater.* **35** 2203836

[40] Tedesco C *et al* 2024 Reaction mechanism of hydrogen generation and nitrogen fixation at carbon nitride/double perovskite heterojunctions *Adv. Energy Sustain. Res.* **5** 2400040

[41] Ricciarelli D, Kaiser W, Mosconi E, Wiktor J, Ashraf M W, Malavasi L, Ambrosio F and De Angelis F 2022 Reaction mechanism of photocatalytic hydrogen production at water/tin halide perovskite interfaces *ACS Energy Lett.* **7** 1308–15

[42] Ricciarelli D, Mosconi E, Wiktor J, Malavasi L, Ambrosio F and De Angelis F 2024 Electron bipolarons at the $DMASnBr_3$–water interface: effect on the photocatalytic hydrogen production *Int. J. Hydrog. Energy* **58** 863–71

[43] Ambrosio F and Wiktor J 2025 Charge localization in optoelectronic and photocatalytic applications: computational perspective *Appl. Phys. Lett.* **126** 130501

[44] Cheng P, Han K and Chen J 2022 Recent advances in lead-free halide perovskites for photocatalysis *ACS Mater. Lett.* **5** 60–78

[45] Chen X, Jia M, Xu W, Pan G, Zhu J, Tian Y, Wu D, Li X and Shi Z 2023 Recent progress and challenges of bismuth-based halide perovskites for emerging optoelectronic applications *Adv. Opt. Mater.* **11** 2202153

[46] Tedesco C and Malavasi L 2023 Bismuth-based halide perovskites for photocatalytic H_2 evolution application *Molecules* **28** 339–58

[47] Islam M, Hadi M and Podder J 2019 Influence of Ni doping in a lead-halide and a lead-free halide perovskites for optoelectronic applications *AIP Adv.* **9** 125321

[48] Schmitz F, Bhatia R, Lamberti F, Meloni S and Gatti T 2023 Heavy pnictogens-based perovskite-inspired materials: sustainable light-harvesters for indoor photovoltaics *APL Energy* **1** 021502

[49] Li M *et al* 2022 Perovskite $Cs_3Bi_2I_9$ hexagonal prisms with ordered geometry for enhanced photocatalytic hydrogen evolution *ACS Energy Lett.* **7** 3370–7

[50] Li N, Zhai X-P, Ma B, Zhang H-J, Xiao M-J, Wang Q and Zhang H-L 2023 Highly selective photocatalytic CO_2 reduction via a lead-free perovskite/MOF catalyst *J. Mater. Chem. A* **11** 4020–9

[51] Baghdadi Y, Temerov F, Cui J, Daboczi M, Rattner E, Sena M S, Itskou I and Eslava S 2023 $Cs_3Bi_2Br_9$/g-C_3N_4 direct Z-scheme heterojunction for enhanced photocatalytic reduction of CO_2 to CO *Chem. Mater.* **35** 8607–20

[52] Derikvand H, Tahmasebi N and Barzegar S 2023 Photocatalytic degradation of organic pollutants under visible light using lead-free all-inorganic halide perovskites A3Bi2Cl9 (A = Cs, Rb) *J. Phys. Chem. Solids* **181** 111528

[53] Azmat S *et al* 2025 A closer look at the interface of $Cs_3Bi_2Br_9$ lead free perovskite in photocatalytic process *J. Phys. Chem. Solids* **199** 112534

[54] Wang C *et al* 2025 Surface and defect engineering coupling of charge shuttle and redox site in $Cs_3Bi_2Br_9$/g-C_3N_4 for efficient photocatalytic C (sp^3)–H bond activation *ACS Mater. Lett.* **7** 610–9

[55] Krajewska C J *et al* 2021 Enhanced visible light absorption in layered $Cs_3Bi_2Br_9$ through mixed-valence Sn (ii)/Sn (iv) doping *Chem. Sci.* **12** 14686–99

[56] Ji Y, She M, Bai X, Liu E, Xue W, Zhang Z, Wan K, Liu P, Zhang S and Li J 2022 In-depth understanding of the effect of halogen-induced stable 2D bismuth-based perovskites for photocatalytic hydrogen evolution activity *Adv. Funct. Mater.* **32** 2201721

[57] Camara J F *et al* 2024 Review of inorganic Sb perovskites and their applications *J. Solid State Chem.* **339** 124943

[58] Biswas A, Rowberg A J, Yadav P, Moon K, Blanchard G J, Kweon K E and Kim S 2024 Ag intercalation in layered $Cs_3Bi_2Br_9$ perovskite for enhanced light emission with bound interlayer excitons *J. Am. Chem. Soc.* **146** 19919–28

[59] Htun T *et al* 2024 Lead-free iron-doped $Cs_3Bi_2Br_9$ perovskite with tunable properties *RSC Adv.* **14** 23177–83

[60] Giovilli G, Albini B, Grisci V, Bonomi S, Moroni M, Mosconi E, Kaiser W, De Angelis F, Galinetto P and Malavasi L 2023 Band gap tuning through cation and halide alloying in mechanochemically synthesized $Cs_3(Sb_1 - xBi_x)_2Br_9$ and $Cs_3Sb_2(I_{1-x}Br_x)_9$ solid solutions *J. Mater. Chem. C* **11** 10282–91

[61] Jiang K, Yang W, Zhang Z, Zhang Y, Lan J, Chen D, Li W and Fan J 2025 Structurally and electronically anisotropic nature of Bridgman-grown $Cs_3Sb_2Br_9$ perovskite single crystal toward efficient photodetector *ACS Appl. Mater. Interfaces* **17** 3631–43

[62] Li S, Song S, Lv P, Wang S, Hong J and Tang G 2025 Enhanced charge transport in a-site ordered perovskite derivatives $A_2A'Bi_2I_9$ (A = Cs; A' = Ag, Cu): a first-principles study *Phys. Chem. Chem. Phys* **27** 14948–56

[63] Miodyńska M, Mikolajczyk A, Mazierski P, Klimczuk T, Lisowski W, Trykowski G and Zaleska-Medynska A 2022 Lead-free bismuth-based perovskites coupled with g-C_3N_4: a machine learning based novel approach for visible light induced degradation of pollutants *Appl. Surf. Sci.* **588** 152921

[64] Shi M, Li G, Tian W, Jin S, Tao X, Jiang Y, Pidko E A, Li R and Li C 2020 Understanding the effect of crystalline structural transformation for lead-free inorganic halide perovskites *Adv. Mater.* **32** 2002137

[65] Liu W, Wu H, Liang T, Miao R, Riaz S and Fan J 2023 Critical roles of octahedron bilayer surface/interior bromide defects in photodynamics of multi-quantum-well-structured cesium bismuth bromide *J. Phys. Chem. Lett.* **14** 5546–52

[66] Li S, Luo J, Liu J and Tang J 2019 Self-trapped excitons in all-inorganic halide perovskites: fundamentals, status and potential applications *J. Phys. Chem. Lett.* **10** 1999–2007

[67] Li J, Wang H and Li D 2020 Self-trapped excitons in two-dimensional perovskites *Front. Optoelectron.* **13** 225–34

[68] Baskurt M and Wiktor J 2023 Charge localization in $Cs_2AgBiBr_6$ double perovskite: small polarons and self-trapped excitons *J. Phys. Chem. C* **127** 23966–72

[69] Dai Z, Lian C, Lafuente-Bartolome J and Giustino F 2024 Excitonic polarons and self-trapped excitons from first-principles exciton-phonon couplings *Phys. Rev. Lett.* **132** 036902
[70] de Paula A M *et al* 2025 Time-domain observation of ultrafast self-trapped exciton formation in lead-free double halide perovskites *J. Am. Chem. Soc.* **147** 28923–31
[71] Baskurt M, Erhart P and Wiktor J 2024 Direct, indirect and self-trapped excitons in $Cs_2AgBiBr_6$ *J. Phys. Chem. Lett.* **15** 8549–54
[72] Jin Y, Rusishvili M, Govoni M and Galli G 2024 Self-trapped excitons in metal-halide perovskites investigated by time-dependent density functional theory *J. Phys. Chem. Lett.* **15** 3229–37
[73] Lazarini F 1977 Caesium enneabromodibismuthate (III) *Acta Crystallogr. B* **33** 2961–4
[74] VandeVondele J, Krack M, Mohamed F, Parrinello M, Chassaing T and Hutter J 2005 Quickstep: fast and accurate density functional calculations using a mixed Gaussian and plane waves approach *Comput. Phys. Commun.* **167** 103–28
[75] Guidon M, Schiffmann F, Hutter J and VandeVondele J 2008 Ab initio molecular dynamics using hybrid density functionals *J. Chem. Phys.* **128** 214104
[76] Guidon M, Hutter J and VandeVondele J 2009 Robust periodic Hartree- Fock exchange for large-scale simulations using Gaussian basis sets *J. Chem. Theory Comput.* **5** 3010–21
[77] Guidon M, Hutter J and VandeVondele J 2010 Auxiliary density matrix methods for Hartree- Fock exchange calculations *J. Chem. Theory Comput.* **6** 2348–64
[78] Miceli G, Chen W, Reshetnyak I and Pasquarello A 2018 Nonempirical hybrid functionals for band gaps and polaronic distortions in solids *Phys. Rev. B* **97** 121112
[79] Bischoff T, Reshetnyak I and Pasquarello A 2019 Adjustable potential probes for band-gap predictions of extended systems through nonempirical hybrid functionals *Phys. Rev. B* **99** 201114
[80] Allen M P and Tildesley D J 2017 *Computer Simulation of Liquids* (Oxford University Press)
[81] Barbara P F, Meyer T J and Ratner M A 1996 Contemporary issues in electron transfer research *J. Phys. Chem.* **100** 13148–68
[82] Matyushov D V 2023 Reorganization energy of electron transfer *Phys. Chem. Chem. Phys* **25** 7589–610
[83] Ambrosio F, Landi A, Loriso M, Leo A and Peluso A 2025 External reorganization energy upon charge transfer reactions in mildly polar media: the case of naphthalene in tetrahydrofuran *J. Phys. Chem. Lett.* **16** 6734–44
[84] Freysoldt C, Neugebauer J and Van de Walle C G 2009 Fully *Ab Initio* finite-size corrections for charged-defect supercell calculations *Phys. Rev. Lett.* **102** 016402
[85] Komsa H-P, Rantala T T and Pasquarello A 2012 Finite-size supercell correction schemes for charged defect calculations *Phys. Rev. B* **86** 045112
[86] Ambrosio F, Wiktor J, De Angelis F and Pasquarello A 2018 Origin of low electron-hole recombination rate in metal halide perovskites *Energy Environ. Sci.* **11** 101–5
[87] Frenkel D and Smit B 2002 *Understanding Molecular Simulation: From Algorithms to Applications* (Academic)
[88] Ambrosio F, Miceli G and Pasquarello A 2015 Redox levels in aqueous solution: effect of van der waals interactions and hybrid functionals *J. Chem. Phys.* **143** 244508
[89] Cheng J and Sprik M 2012 Alignment of electronic energy levels at electrochemical interfaces *Phys. Chem. Chem. Phys.* **14** 11245–67
[90] Costanzo F, Sulpizi M, Valle R G D and Sprik M 2011 The oxidation of tyrosine and tryptophan studied by a molecular dynamics normal hydrogen electrode *J. Chem. Phys.* **134** 244508
[91] Sulpizi M and Sprik M 2008 Acidity constants from vertical energy gaps: density functional theory based molecular dynamics implementation *Phys. Chem. Chem. Phys* **10** 5238–49
[92] Falletta S, Wiktor J and Pasquarello A 2020 Finite-size corrections of defect energy levels involving ionic polarization *Phys. Rev. B* **102** 041115
[93] Strand J, Chulkov S K, Watkins M B and Shluger A L 2019 First principles calculations of optical properties for oxygen vacancies in binary metal oxides *J. Chem. Phys.* **150** 044702
[94] Iannuzzi M, Chassaing T, Wallman T and Hutter J 2005 Ground and excited state density functional calculations with the Gaussian and augmented-plane-wave method *Chimia* **59** 499
[95] Bratsch S G 1989 Standard electrode potentials and temperature coefficients in water at 298.15 K *J. Phys. Chem. Ref. Data* **18** 1–21
[96] Alexandrov A S and Devreese J T 2010 *Advances in Polaron Physics* vol 159 (Springer)
[97] Small D W, Matyushov D V and Voth G A 2003 The theory of electron transfer reactions: what may be missing? *J. Am. Chem. Soc.* **125** 7470–8
[98] Böttger H and Bryksin V V 1985 *Hopping Conduction in Solids* (De Gruyter)
[99] Blumberger J 2015 Recent advances in the theory and molecular simulation of biological electron transfer reactions *Chem. Rev.* **115** 11191–238
[100] Houmsi H, Sklénard B, Guillaumont M, Triozon F and Li J 2025 Revisiting the extraction of coupling strengths for polaron hopping from an ab initio approach *Phys. Rev. B* **111** 165147
[101] Marcus R A 1993 Electron transfer reactions in chemistry: theory and experiment (Nobel Lecture) *Angew. Chem. Int. Ed.* **32** 1111–21
[102] Marcus R A 1964 Chemical and electrochemical electron-transfer theory *Annu. Rev. Phys. Chem.* **15** 155–96
[103] Holstein T 1959 Studies of polaron motion: Part II. The "small" polaron *Ann. Phys.* **8** 343–89
[104] Emin D and Holstein T 1969 Studies of small-polaron motion IV. Adiabatic theory of the Hall effect *Ann. Phys.* **53** 439–520
[105] Austin I and and N M 1969 Polarons in crystalline and non-crystalline materials *Adv. Phys.* **18** 41–102
[106] Wu F and Ping Y 2018 Combining Landau–Zener theory and kinetic Monte Carlo sampling for small polaron mobility of doped $BiVO_4$ from first-principles *J. Mater. Chem. A* **6** 20025–36
[107] Palermo G, Falletta S and Pasquarello A 2024 Migration of hole polarons in anatase and rutile TiO_2 through piecewise-linear functionals *Phys. Rev. B* **110** 235205
[108] Böttger H and Bryksin V V 2022 *Hopping Conduction in Solids* (De Gruyter)
[109] Henkelman G, Uberuaga B P and Jónsson H 2000 A climbing image nudged elastic band method for finding saddle points and minimum energy paths *J. Chem. Phys.* **113** 9901–4
[110] Wang Z and Bevan K H 2016 Exploring the impact of semicore level electronic relaxation on polaron dynamics: an adiabatic ab initio study of $FePO_4$ *Phys. Rev. B* **93** 024303
[111] Alkauskas A, Lyons J L, Steiauf D and Van de Walle C G 2012 First-principles calculations of luminescence spectrum line shapes for defects in semiconductors: the example of GaN and ZnO *Phys. Rev. Lett.* **109** 267401

[112] Alkauskas A, Yan Q and Van de Walle C G 2014 First-principles theory of nonradiative carrier capture via multiphonon emission *Phys. Rev. B* **90** 075202
[113] Battaile C C 2008 The Kinetic Monte Carlo method: foundation, implementation and application *Comput. Methods Appl. Mech. Eng.* **197** 3386–98
[114] Landi A, Landi A, Velardo A and Peluso A 2022 Efficient charge dissociation of triplet excitons in bulk heterojunction solar cells *ACS Appl. Energy Mater.* **5** 10815–24
[115] Padula D, Barneschi L, Peluso A, Cinaglia T and Landi A 2023 Towards a fast machine-learning-assisted prediction of the mechanoelectric response in organic crystals *J. Mater. Chem. C* **11** 12297–306
[116] Landi A, Ambrosio F, Leo A, Padula D, Prampolini G and Peluso A 2025 Effect of thermal disorder on the electronic structure and the charge mobility of acenes *ChemRxiv* (available at: https://chemrxiv.org/engage/chemrxiv/article-details/67fcbeed6dde43c908cc1099) (Accessed 14 May 2025)
[117] Einstein A 1956 *Investigations on the Theory of the Brownian Movement* (Courier Corporation)
[118] Ouhbi H and Wiktor J 2021 Polaron formation and hopping in tantalate perovskite oxides: $NaTaO_3$ and $KTaO_3$ *Phys. Rev. B* **104** 235158
[119] Baghdadi Y, Daboczi M, Temerov F, Yang M, Cui J and Eslava S 2024 A g-C_3N_4/rGO/$Cs_3Bi_2Br_9$ mediated Z-scheme heterojunction for enhanced photocatalytic CO_2 reduction *J. Mater. Chem. A* **12** 16383–95
[120] Stippell E, Li W, Quarti C, Beljonne D and Prezhdo O V 2024 Enhancing interlayer charge transport of two-dimensional perovskites by structural stabilization via fluorine substitution *ACS Appl. Mater. Interfaces* **17** 2032–40
[121] Yan L, Ma J, Li P, Zang S, Han L, Zhang Y and Song Y 2022 Charge-carrier transport in quasi-2D Ruddlesden–Popper perovskite solar cells *Adv. Mater.* **34** 2106822